

Site-specifically tailored microstructures with enhanced strength and hardening through laser powder bed fusion

C. Sofras^{a,b}, J. Čapek^a, X. Li^c, C.C. Roth^c, C. Leinenbach^{d,e}, R.E. Logé^b, M. Strobl^a, E. Polatidis^{a,*}

^a Paul Scherrer Institut, Laboratory for Neutron Scattering and Imaging, 5232 Villigen, Forschungsstrasse 111, Switzerland

^b Thermomechanical Metallurgy Laboratory (LMTM) – PX Group Chair, École Polytechnique Fédérale de Lausanne (EPFL), CH-2002 Neuchâtel, Switzerland

^c Chair of Computational Modeling of Materials in Manufacturing, Department of Mechanical and Process Engineering, ETH, Zurich, Switzerland

^d Empa, Swiss Federal Laboratories for Materials Science and Technology, 8600 Dübendorf, Switzerland

^e Laboratory for Photonic Materials and Characterization, École Polytechnique Fédérale de Lausanne, 1015 Lausanne, Switzerland

ARTICLE INFO

Keywords:

Additive manufacturing
Stainless steel
Deformation twinning
Mechanical behavior

ABSTRACT

Laser powder bed fusion (L-PBF) has emerged as an additive manufacturing technique that offers unprecedented design freedom. Besides being capable of producing complex and near net shape objects, L-PBF can impact tremendously the engineering materials community due to the possibility of locally manipulating metallic microstructures. Here we exploit the latter potentiality of L-PBF, to produce site-specifically tailored stainless steel components, in terms of their crystallographic texture. The tailored materials are tested and exhibit superior energy dissipation capabilities under bending deformation compared to uniformly textured materials. This is enabled by the strong dependence of the secondary hardening mechanisms, namely the deformation twinning and/or martensite formation, of these materials on the locally tuned microstructures. With the aid of finite element simulations, it is possible to identify the stress state and hence, the crystallographic orientations that facilitate twinning or martensite formation. Then, by engineering favorable crystallographic textures, matched to the complex stress state during bending, enhanced work hardening behavior is obtained. This site-specific microstructure design enabled by L-PBF provides a new pathway for the design of “smart” components that exhibit superior mechanical response under complex stress states.

1. Introduction

Besides the possibility of designing near net-shape parts with highly complex geometries, metal additive manufacturing (AM) is a powerful tool for producing tailored microstructures [1–4]. By carefully adjusting the process parameters, the solidification conditions can be altered that in turn can strongly affect the obtained microstructures [5,6]. As such, there have been several studies showing that “monolithic”, i.e. uniform microstructures, can exhibit superior mechanical [6–10] or functional properties [11,12] than conventional microstructures. A unique possibility of AM is that the microstructure can be manipulated within a single component, enabling in this way parts with locally altered microstructures and consequently a tailored combination of different mechanical properties. This potentiality bears the promise of revolutionizing the design of engineering components, as site-specific tailoring of microstructures is impossible with conventional metal

processing techniques.

Until today, some researchers have explored the possibility of tailoring microstructures with AM, with the aim of creating functionally variable components, in different alloy systems [13–15]. Sofinowski et al. [16] produced cubes with controlled crystallographic texture, perpendicular to the building direction (BD), from a 316L austenitic stainless steel. By keeping a constant crystallographic texture of {101} along the BD and by rotating the laser scanning angle, the texture in the plane perpendicular to the BD can be manipulated. It has been demonstrated that this method can be exploited in order to develop microstructures with encrypted messages, which can be revealed by characterizing the crystallographic texture, such as written messages or QR codes [17,18]. Additionally, it has been demonstrated that adoption of different scanning strategies can lead to the formation of regions within the microstructure with different phase composition [19] or grain size and crystallographic texture. Rescanning or remelting specific

* Corresponding author.

E-mail address: efthymios.polatidis@psi.ch (E. Polatidis).

<https://doi.org/10.1016/j.matdes.2023.112539>

Received 23 June 2023; Received in revised form 15 October 2023; Accepted 3 December 2023

Available online 5 December 2023

0264-1275/© 2023 The Author(s). Published by Elsevier Ltd. This is an open access article under the CC BY license (<http://creativecommons.org/licenses/by/4.0/>).

regions of the sample has also been shown to greatly affect the phase composition of the as-built sample as it can lead to the evaporation of certain elements, affecting the stability of certain phases at room temperature [20,21]. However, until now, site-specific microstructures, in terms of their crystallographic texture, were never explored for the development of mechanically superior materials under conditions that resemble real-world applications. This shall be explored for the first time in the present study on two austenitic steel grades under a complex stress state, namely V-bending which exhibits a gradient of plane strain tension to plane strain compression within one component. As such, the applied methodology lays the foundations for applying the principle onto variable complex stress states during deformation of lattice structures or open cells structures.

The crystallographic texture manipulation capabilities of L-PBF relies on two basic principles. The first one is the preferential solidification of metals and alloys with cubic crystal structure. Thus, it has been observed that the $\langle 001 \rangle$ crystallographic direction aligns with the direction of the thermal gradient in e.g. a 316L stainless steel processed by LPBF [22]. The second phenomenon is the fact that epitaxial growth of existing grains is energetically more favorable than the nucleation of new grains [23]. Due to the distinct curved geometry of the melt pool during the L-PBF process, the thermal gradient within the melt pool is inclined at approximate $\pm 45^\circ$ orientation with respect to the BD. As such, the solidified grains align along their $\langle 001 \rangle$ direction at approximately $\pm 45^\circ$ with respect to the BD and ultimately, due to the cubic structure, their $\langle 101 \rangle$ direction aligns along the BD. Since epitaxial growth is favored over nucleation of new grains when a subsequent melt pool overlaps with an already solidified one, the new cells will grow along the $\langle 001 \rangle$ of the already existing cells, aligning again their $\langle 101 \rangle$ directions with the BD [11,16,24,25]. Moreover, the epitaxial growth that is induced by the bi-directional scanning strategy, within the same layer, leads to the alignment of the $\langle 001 \rangle$ direction of the cells along the scanning direction [16]. As such, by aligning the scanning angle accordingly, it is possible to engineer the crystallographic texture along a desired direction of the sample; i.e. when the scanning direction is parallel to the desired direction, then $\langle 001 \rangle$ texture is achieved and when the scanning direction is at 55° to the desired direction, then $\langle 111 \rangle$ texture is achieved.

In the present investigation, we exploit the possibility of site-specific engineering of the crystallographic texture with L-PBF, in order to produce tailored metallic microstructures of 316L or 304L that exhibit enhanced mechanical response under V-bending deformation. V-bending is a well-established mechanical testing technique [26] that is critical for crash applications. Upon loading, the convex part of the specimen is subjected to plane strain tension (hereafter denoted as the tensile side) while the concave part of the specimen is subjected to plane strain compression (hereafter denoted as the compressive side). In addition, a region across the centerline of the sample remains undeformed (hereafter denoted as the neutral section).

The conception of the tailored structures presented in this investigation lies in the dependence of the strain hardening phenomena on the crystallographic texture along the direction of the applied load. The grades of 316L and 304L stainless steels have been a focal point of interest in the additive manufacturing community, not only for their excellent printability, but also for their excellent combination of strength and ductility [6,8,27–29]. Upon plastic deformation, 316L exhibits extensive deformation twinning as the dominant deformation mechanism due to its low enough stacking fault energy; the so-called twinning induced plasticity effect - TWIP. Therefore, the TWIP effect results in a well-balanced combination of strength and ductility, due to the dynamic Hall-Petch effect, because the twin boundaries act as grain boundaries, reducing the dislocation mean-free path [30,31]. On the other hand the 304L typically exhibits the Transformation Induced Plasticity (TRIP) or a combination of the TRIP and TWIP effects [32,33].

It has been theoretically [34,35] and experimentally verified [36–39] that, depending on the loading state, certain crystallographic

textures along the loading direction promote the TWIP effect, while others suppress it. More specifically, the TWIP effect is governed by the dissociation of a perfect $a/2 \langle 110 \rangle$ dislocation into two $a/6 \langle 112 \rangle$ Shockley partial dislocations, which are referred to as leading and trailing partial dislocations (hereafter denoted as LPD and TPD accordingly) [35,39,40]. The Shockley partials glide on the $\{111\}$ planes of the FCC lattice, and they are separated by a stacking fault. Upon the application of external load, the partials separate and form extensive stacking faults. The accumulation of stacking faults on every parallel $\{111\}_\gamma$ plane leads to the formation of twins. As such, by considering the resolved shear stress on both leading and trailing partial dislocation, which have the same slip plane but different Burger's vectors, via the Schmid factor, it is seen that the extent of the dissociation of the partial dislocations is dependent on the orientation, under the application of external load. Hence, the formation of twins within individual grains is governed by their crystallographic orientation with respect to the loading direction. Under uniaxial tensile deformation, orientations close to the $\langle 111 \rangle$ axis are thus considered “favorable” and close to the $\langle 001 \rangle$ axis are considered “unfavorable” for the TWIP effect and vice-versa under uniaxial compression [39–41]. Under biaxial stress state, the favorable orientations are different [42] and moreover every stress state has to be considered thoroughly with respect to the desired crystallographic textures. Such prior knowledge is essential for designing materials that are produced by AM and experience complex stress state.

Here we show that by engineering bimodal 316L components with L-PBF, where both the tensile and compressive sides of V-bending specimens exhibit different but both either “favorable” or “unfavorable” crystallographic textures, it is possible to strongly enhance or strongly suppress the TWIP effect – simultaneously on the whole deformed area of the component. The design of the microstructure is done with the aid of finite element simulation and the Taylor model to simulate the evolving deformation texture. When bending a favorably engineered component, it is possible to trigger a massive TWIP effect and to markedly increase the energy dissipation capacity, compared to a uniform microstructure and more significantly to an unfavorably engineered microstructure. The applicability of the method is underlined by using the exact same process parameters amongst all samples but only changing the laser scanning direction with respect to the sample coordinate system. Moreover, the investigation is extended to a 304L stainless steel, which exhibits a combination of TWIP and transformation induced plasticity (TRIP).

2. Materials and methods

2.1. FE simulation

Finite element simulations using ABAQUS/Explicit were performed to model the stress and strain distribution across the thickness of the samples during V-bending. The model used in the present investigation was developed and optimized (in terms of element size, element type and convergence analysis) in the context of the publication by Roth et al. [43]. A schematic of the V-bending test is shown in Fig. 1. For computational efficiency, half of the part (i.e. 30 mm in length, 20 mm in width and 2 mm in thickness) was modelled using symmetry boundary conditions on appropriate surfaces. The simulation was run on a “favorable” arrangement of texture. It should be noted that the stress and strain distribution, in a simulated arrangement of an “unfavorable” sample did not differ significantly. It is noted that the terms “favorable” and “unfavorable” samples are explained in section 2.3. Eight node reduced integration brick elements were used, 200 along the width of the sample and 20 along its thickness. It should be noted that isotropic mechanical properties were considered in the model for the sake of simplicity.

2.2. Design of the microstructure

Fig. 1a and b show the distribution of the 3 principal stress and strain

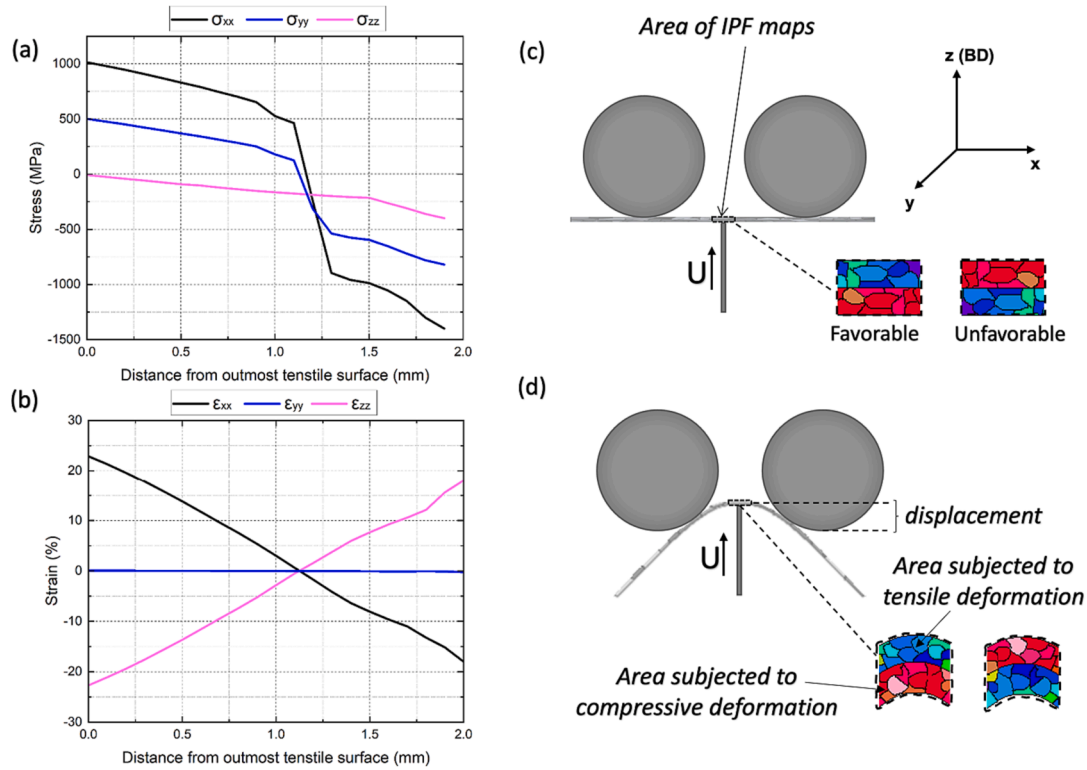


Fig. 1. (a) Finite Element simulation of the stress components in the central region across the thickness of the sample. (b) Finite Element simulation of the strain components in the central region across the thickness of the sample for a V-bending test at 6 mm. (c),(d) Schematic representation of the V-bending test depicting a moving anvil (displacement controlled) moving along direction U and two fixed supports, for both initial and deformed states. The deformed schematic depicts the setup for deforming either a favorable or unfavorable sample, where either the tensile side or the compression side have strong $\langle 111 \rangle$ or $\langle 001 \rangle$ in-plane crystallographic textures. The dashed line schematically shows the cross section in which EBSD studies are undertaken, covering the entire thickness of the samples in both deformed and undeformed samples.

components along the thickness of the sample, at the central region of the sample for 6 mm of displacement of the anvil (see section 2.4). Fig. 1a shows that on one side, the longitudinal stress component, σ_{xx} , exhibits the highest value. The transverse stress component, σ_{yy} , exhibits half the value of σ_{xx} , while the out of plane component, σ_{zz} , is negligible. On the opposite side, the σ_{xx} , and σ_{yy} stress components exhibit the same trend as on the tensile side. However, the out of plane component σ_{zz} exhibits a relatively high value, reaching a quarter of the value of σ_{xx} . Fig. 1b shows the distribution of strains at the central region of the sample. The longitudinal strain component ϵ_{xx} is tensile in the tensile side, which gradually shifts to compression on the opposite side of the sample (i.e., the compressive side). On the other hand, the out of plane strain component ϵ_{zz} shows the exact opposite trend, compared to ϵ_{xx} . Lastly, the transverse strain component, ϵ_{yy} remains zero throughout the thickness of the sample. Taking the above into account, during the V-bending test the sample is subjected to a stress state that on both the tensile and compressive sides resemble the plane strain stress state. Fig. S1 of the supplementary shows the results of the FE model at higher displacements showing the evolution of the stress state. It can be observed that as the deformation level gets larger, the stress state remains the same. It should be noted that the FE simulations results corroborate well with previous work on V-bending in [44].

As it has been outlined in the introduction, the TWIP effect is orientation-dependent and related to the ability of the applied load to create stacking faults, i.e., when the Schmid factor of the leading partial dislocation is higher than the Schmid factor of the trailing partial dislocation. The application of the Schmid law on the leading and trailing partial dislocations under uniaxial tension and compression has been demonstrated [33]; however in the case of plane strain, the favorable or unfavorable orientations need to be reevaluated. Therefore,

in order to identify the crystallographic orientations that enhance the TWIP effect we calculated the difference in the Schmid factor of the leading and trailing partial dislocations, for the perfect slip system with the highest Schmid factor under plain strain conditions. This was done by considering 2000 grains with random crystallographic orientation and by applying the stress tensor of the outermost element at 6 mm displacement as shown in Fig. 1, using the MTEX toolbox [45]. Two simulations were undertaken, corresponding to the tensile and compressive sides respectively. The MTEX script that performs the simulation for any given stress tensor, is provided in the open data repository, so that any stress state can be simulated. Fig. 2a and b show the orientation dependence in the difference between the Schmid factor of the leading and trailing partial dislocations, plotted in Inverse Pole Figures (IPFs) with respect to the x-direction (see Fig. 1). For the tensile side, it is observed that orientations close to the $\langle 101 \rangle$ pole, close to the $\langle 111 \rangle$ pole and with orientations between these two, have the highest difference in the value of the Schmid factor of the partial dislocations, i.e. they favor the TWIP effect. On the other hand, for the compressive side, orientations very close to the $\langle 001 \rangle$ pole favor the TWIP effect. As such, it is evident that an arrangement of a $\langle 101 \rangle$ or $\langle 111 \rangle$, along the x direction, on the tensile side with a $\langle 001 \rangle$, along the x direction, on the compressive side, enhances the TWIP effect along the whole sample.

Besides the initial crystallographic texture, the evolving deformation texture affects the TWIP or TRIP effect, as already shown [33,46]. For this reason, we used the Taylor model implementation in the MTEX toolbox [45] in order to follow the evolution of the crystallographic texture during the V-bending test on the tensile and compressive sides. For the simulation an initially random crystallographic texture, comprised of 2000 grains, was subjected to the same strains that were obtained by the finite element analysis. The MTEX script that performs the simulation for any given strain tensor, is provided in the open data

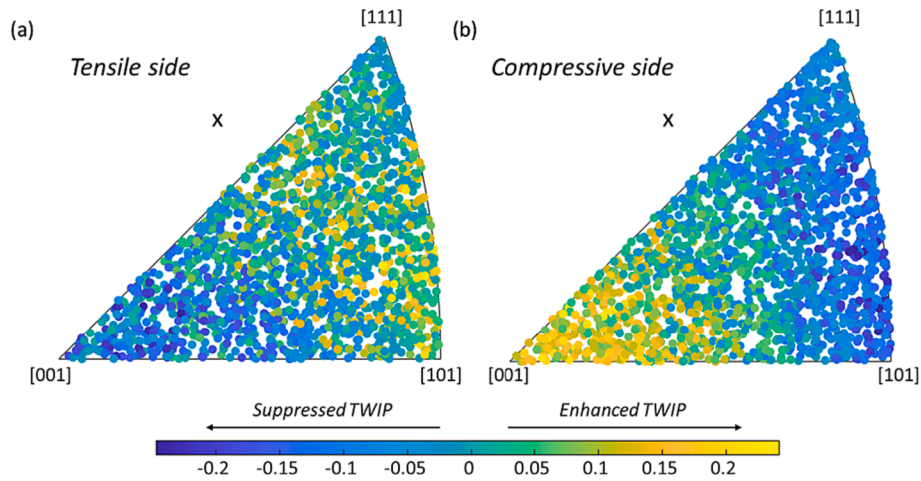


Fig. 2. Simulation results IPF triangles with respect to the x-direction showing the difference in the Schmid factor between the leading and trailing partial dislocation for (a) on the tensile side and (b) on the compressive side.

repository. Fig. 3a and b show the evolution of a random crystallographic texture, at different levels of displacements of the anvil, for the tensile and the compressive sides, accordingly. The results are represented with inverse pole figures with respect to the x-direction. It is observed that on the tensile side, a strong nearly $\langle 111 \rangle$ crystallographic texture forms along the x-direction while the deformation progresses. On the other hand, on the compressive side a strong $\langle 101 \rangle$ crystallographic texture forms along the x-direction.

By considering the dependency of the TWIP effect on the stress state and on the evolving crystallographic texture under plane strain stress state in both tensile and compressive sides, we identify the favorable orientations for TWIP effect. As such, strong $\langle 111 \rangle$ on the tensile side and $\langle 001 \rangle$ on the compressive side along the x-direction is the most suitable arrangement for enhanced TWIP or/and TRIP effects during the V-bending test.

2.3. Sample preparation

For the L-PBF process gas atomized 316L and 304L powders with maximum particle size of $45 \mu\text{m}$, purchased from Carpenter Additive UK, were used. Samples with dimensions of $60 \times 20 \times 10 \text{ mm}^3$ were manufactured using a Sisma MySint 100 with a spot size of $55 \mu\text{m}$, under argon atmosphere ($<300 \text{ ppm}$ oxygen in circulation during printing). We set the laser power for all samples to 175 W, the scanning speed to 1000 mm/s, the hatch spacing to $80 \mu\text{m}$ and the layer thickness to $30 \mu\text{m}$.

Bimodal samples, i.e. samples exhibiting two distinct crystallographic textures, were manufactured from either powder. The sample denoted as “favorable” was manufactured so as to exhibit a $\langle 111 \rangle$ crystallographic texture along the x-direction on the tensile side. In addition, the sample exhibits a $\langle 001 \rangle$ crystallographic texture along the x-direction on the compressive side. The sample denoted as

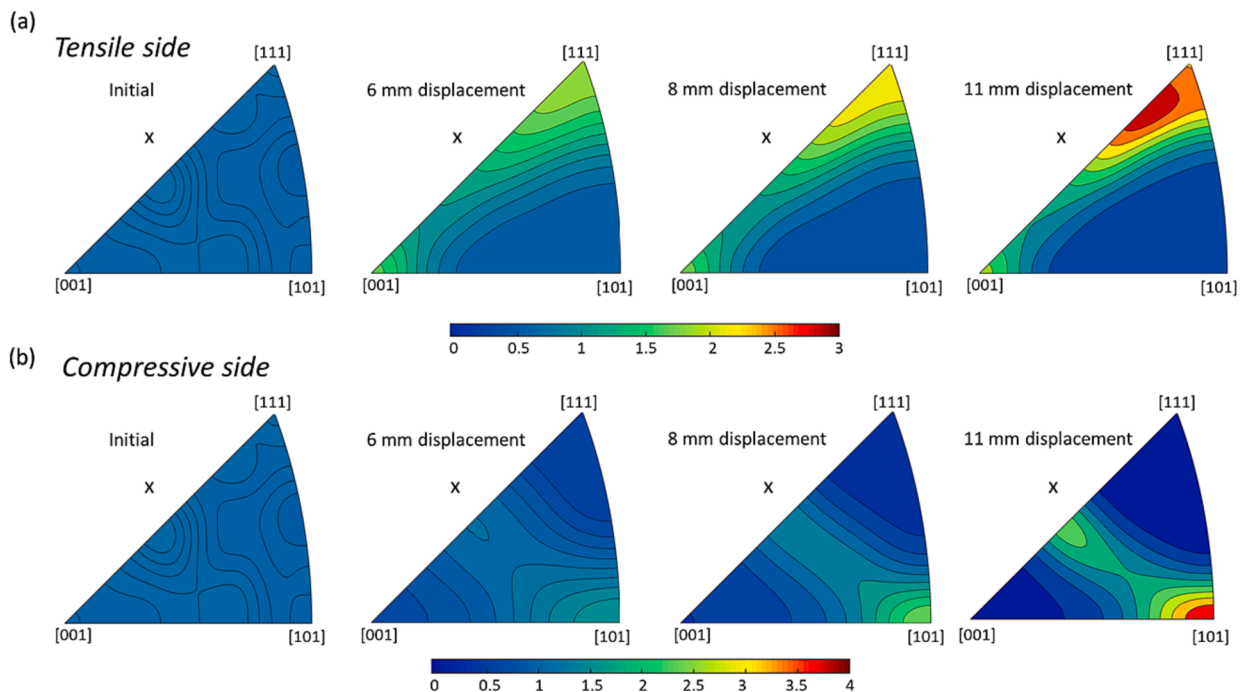


Fig. 3. Simulation results showing the evolution of the crystallographic texture with respect to the x-direction (see Fig. 1) during V-bending deformation (a) on the tensile side and (b) on the compressive side.

“unfavorable” was manufactured in the exact same way as the favorable sample, however by reversing the bending direction during the V-bending test. Therefore, the “unfavorable” sample exhibits a $\langle 111 \rangle$ crystallographic texture along the x-direction on the compressive side and a $\langle 001 \rangle$ crystallographic texture along the x-direction on the tensile side. To highlight the importance of tailoring the microstructure to the mechanical behavior, three “monolithic” 316L samples were produced. One “monolithic” sample with nearly random crystallographic texture, and two more “monolithic” samples with strong $\langle 111 \rangle$ and $\langle 001 \rangle$ along the x-direction, denoted hereafter as “M111” and “M001” respectively.

All layers of the favorable and unfavorable samples were printed using a bi-directional scanning pattern. The first 167 layers were printed with a laser scanning angle of 0 with respect to the x-direction, for manufacturing $\langle 001 \rangle$ texture along the x-direction. The remaining layers were printed with a laser scanning angle of 55° with respect to the x-direction, for manufacturing $\langle 111 \rangle$ texture along the x-direction. For the monolithic samples either a 0 or a 55° scanning angle was used with respect to the x-direction throughout the building process. The randomly-textured 316L sample was manufactured with the exact same process parameters, by using a uni-directional scanning strategy with 67° rotation between subsequent layers. The samples were extracted in the appropriate thickness for the V-bending test (i.e. 2 mm) by electrical discharge machining (EDM). As such, the bimodal samples comprised of a 1 mm thick section with $\langle 111 \rangle$ and a 1 mm thick section with $\langle 001 \rangle$ crystallographic texture in the x-direction direction.

It is noted that since all samples in the present investigation are manufactured with the exact same process parameters and with the exact same build tasks (i.e. number of samples per task, waiting time between subsequent layers, recoater moving speed), the effect of the solidification cells, chemical segregation and grain size are not considered to attribute in the observed differences in the mechanical behavior of the samples, which is presented in section 3.

2.4. Mechanical testing

V-bending tests were carried out using the setup established in the

investigation by Roth et al. [43]. The tests were performed with the anvil moving at a speed of 2 mm/min until a maximum anvil displacement of 6 mm, 8 mm and 11 mm was reached for all samples. To assess the reproducibility of the results, two favorable and two unfavorable samples were deformed until a maximum displacement of 11 mm, while either favorable or unfavorable samples were tested until 6 mm and 8 mm anvil displacements for microscopy characterization in intermediate strains. All test results exhibit excellent reproducibility, as shown in Fig. S2 in the supplementary section. The dimensions of the sample used for the V-bending tests were $60 \times 20 \times 2 \text{ mm}^3$. Fig. 1c and d show a schematic representation of the V-bending test setup used for the investigation. For the detailed EBSD investigation, additional favorable and unfavorable 316L samples were deformed until a total displacement of the anvil of either 6 mm or 8 mm.

2.5. Microstructural characterization

The deformed 316L samples were cut in half of their width with EDM. The cross-section of the samples was ground until 4000 grit SiC paper and then electropolished using a 16:3:1 (by volume) ethanol, glycerol and perchloric acid solution at 50 V for 10 s. A field emission gun scanning electron microscope (FEG SEM) Zeiss Ultra 55 equipped with an EDAX Hikari camera operating at 20 kV accelerating voltage, was used for the EBSD measurements. The step size used for the EBSD maps was set to $0.5 \mu\text{m}$. The raw EBSD maps were collected and then post-processed using the commercial software TSL OIM Analysis 8.

3. Results and discussion

Fig. 4a shows an EBSD orientation map with inverse pole figure (IPF) coloring of the bimodal sample, with respect to the x-direction, in the as-built state, along with the corresponding pole figures (PFs). The sample has two distinct, differently textured sections across its thickness depending on the scanning direction with respect to the x-direction, as explained in the experimental section. For both sections, the sample exhibits a strong $\langle 101 \rangle$ crystallographic texture along the BD. In terms

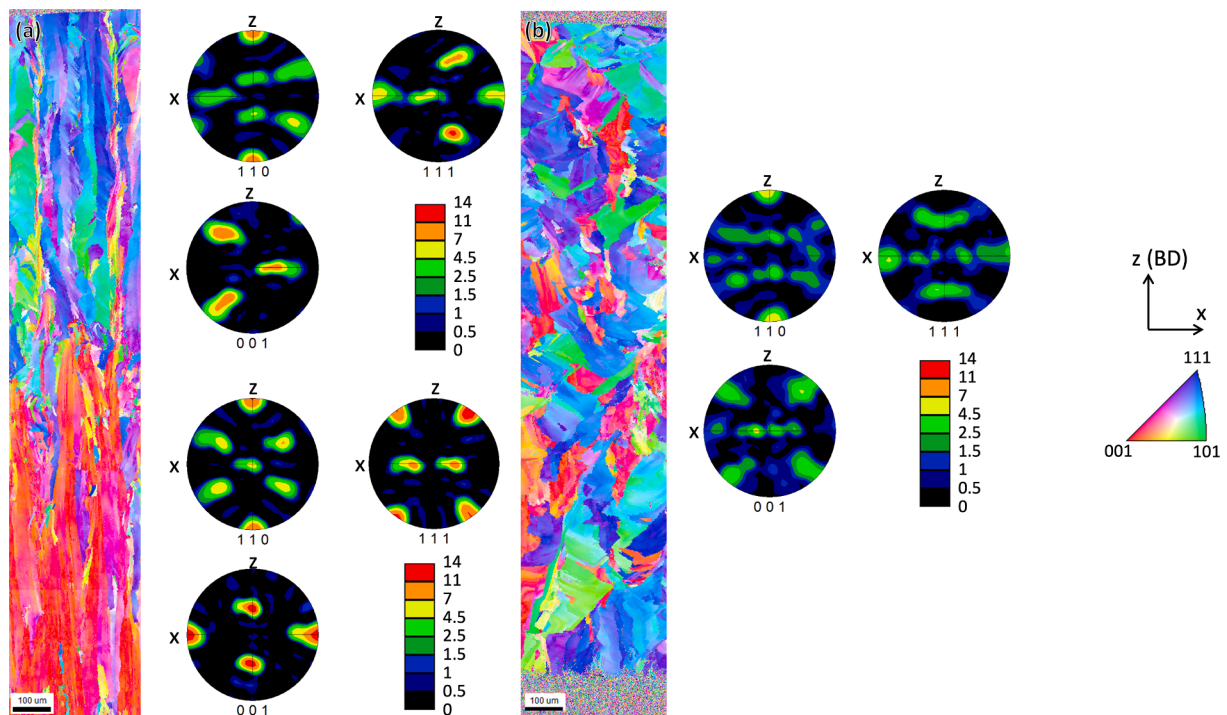


Fig. 4. EBSD orientation map with IPF coloring along the x-direction of the as-built state and the corresponding pole figures of the (a) bimodal samples showing the two distinct sides of the sample, (b) the uniform “monolithic” sample with random crystallographic texture.

of grain morphology, the sample exhibits the typical elongated grains along the BD that are characteristic of L-PBF microstructures [11,16,28]. The width of the transition zone is approximately 250 μm , determined by the average grains misorientation along the thickness of the sample (Fig. S3 of the supplementary materials section). Fig. 4b shows an EBSD orientation map with IPF coloring of the randomly textured sample, with respect to the x-direction, in the as-built state, along with the corresponding PFs. The sample exhibits a much less pronounced crystallographic texture along the x-direction compared to the bimodal samples. Additionally, it is characterized by relatively more equiaxed grains, compared to the elongated grains of the bimodal samples.

Fig. 5a shows the normalized force–displacement curves of five 316L L-PBF samples, after the V-bending test. The force is normalized by the thickness of each sample, in order to account for slight thickness variations due to manufacturing tolerances. For all samples, the force until yielding and early during the plastic regime, is nearly identical, except for the M111 sample that exhibits a slightly higher yield point resembling the mechanical behavior of the corresponding lattice families [33]. Later in the plastic regime, the mechanical response of the samples differs significantly. The favorable sample exhibits the steepest work hardening among the samples, while the unfavorable sample the most moderate, despite the fact that both samples have been manufactured identically. The random and the monolithic samples, exhibit nearly similar behavior due to a similar on average TWIP activity throughout the tensile and compression sides of the sample, i.e. due to the existence of a balanced population of favorable and unfavorable grains. Fig. 5b shows the maximum specific energy absorption of the five samples after bending them at 11 mm displacement, which is calculated by integrating the force–displacement curve and dividing by the mass of the sample [47]. The favorable sample exhibits up to 30 % higher ultimate normalized force and up to 20 % higher total energy absorption during the course of bending, compared to the unfavorable sample.

To verify the significant difference of the mechanical behavior of two otherwise identical samples with the extreme behaviors, the microstructure of the entire cross-section was investigated in a series of favorable and unfavorable samples at different anvil displacements. The EBSD maps cover the entire cross-section of the samples, as schematically shown in Fig. 1. Fig. 6 shows EBSD orientation maps with IPF coloring, with respect to the x-direction, and image quality maps with the deformation twin boundaries highlighted with red, for the favorable and unfavorable samples at 6 mm, 8 mm and 11 mm displacement. The elongated grain structure along the building direction, typical of the L-

PBF process [11,16,28], is observed at all stages of deformation. During the deformation process, twins develop, as highlighted with red lines in Fig. 6. Additionally, the deformation textures that are predicted by the Taylor model (Fig. 3), i.e. $\langle 111 \rangle$ along the x-direction on the tensile side and $\langle 101 \rangle$ along the x-direction on the compressive side, are also observed.

Most importantly, it is found that the favorable 316L sample exhibits a significantly more pronounced TWIP effect than the unfavorable sample. Fig. 7 shows the line fraction of the deformation twin boundaries relative to all grain boundaries across the thickness of the samples, binned in 0.25 mm thick areas, across the sample's thickness. At 6 mm displacement, where the difference of the force–displacement curves of the favorable and unfavorable samples is still relatively small, the favorable sample exhibits already an apparently higher density of deformation twins, than the unfavorable sample, both in tensile and on the compressive side. At 8 mm displacement, the density of deformation twins in the favorable sample increases significantly more than in the unfavorable sample, and hence the difference in the mechanical response of the two samples becomes more pronounced. Finally, at 11 mm displacement the TWIP effect is significantly more pronounced in the favorable sample, as the line fraction becomes 5 times larger, than in the unfavorable sample, in both the tensile and compressive sides.

The reason of the different mechanical behavior of the identical samples when bending them in the opposite directions lies in the dependence of the TWIP effect on the crystallographic texture and the corresponding stress state, as shown in Fig. 2. Therefore, L-PBF offers the opportunity to produce parts with favorable textures for twinning in both their tensile and compressive sides during bending and achieve superior mechanical properties than monolithic samples. When the bending direction is reversed, i.e. the unfavorable sample, then both tensile and compressive sides suppress twinning and the mechanical properties are inferior compared to monolithic samples.

Fig. 8 shows details of the twin structure, in high magnification EBSD orientation maps, along the x-direction, with IPF coloring and image quality maps with the deformation twin boundaries highlighted red for the favorable and unfavorable samples at 8 mm displacement. It can be seen that a massive TWIP effect is triggered in grains with blue IPF color and in grains with red IPF color on the tensile side and on the compressive side, respectively, in the favorable sample. The twins become more dense and thicker with increasing deformation as shown in Fig. 9a–c. In the unfavorable grains, strain is accommodated by dislocation slip, which can be observed by the color variation in the

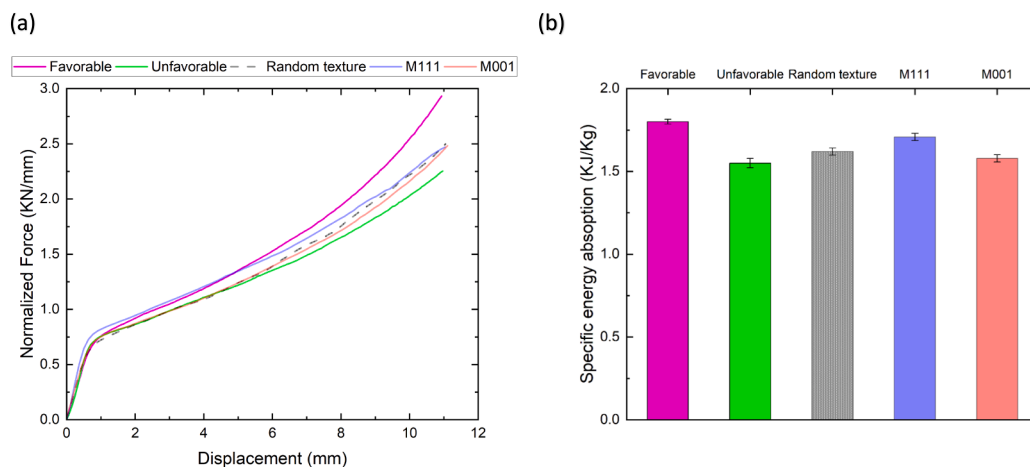


Fig. 5. Mechanical behavior (experimental data) of the L-PBF 316L stainless steel samples upon V-bending deformation. (a) Normalized force–displacement curves for the favorable, unfavorable, random-textured, $\langle 111 \rangle$ and $\langle 001 \rangle$ textured samples. (b) Total dissipated energy shown as specific energy absorption at the end of deformation (until 11 mm displacement) for the favorable, unfavorable, random-textured, $\langle 111 \rangle$ and $\langle 001 \rangle$ textured samples. The error bars represent the standard deviation among measurements for each sample.

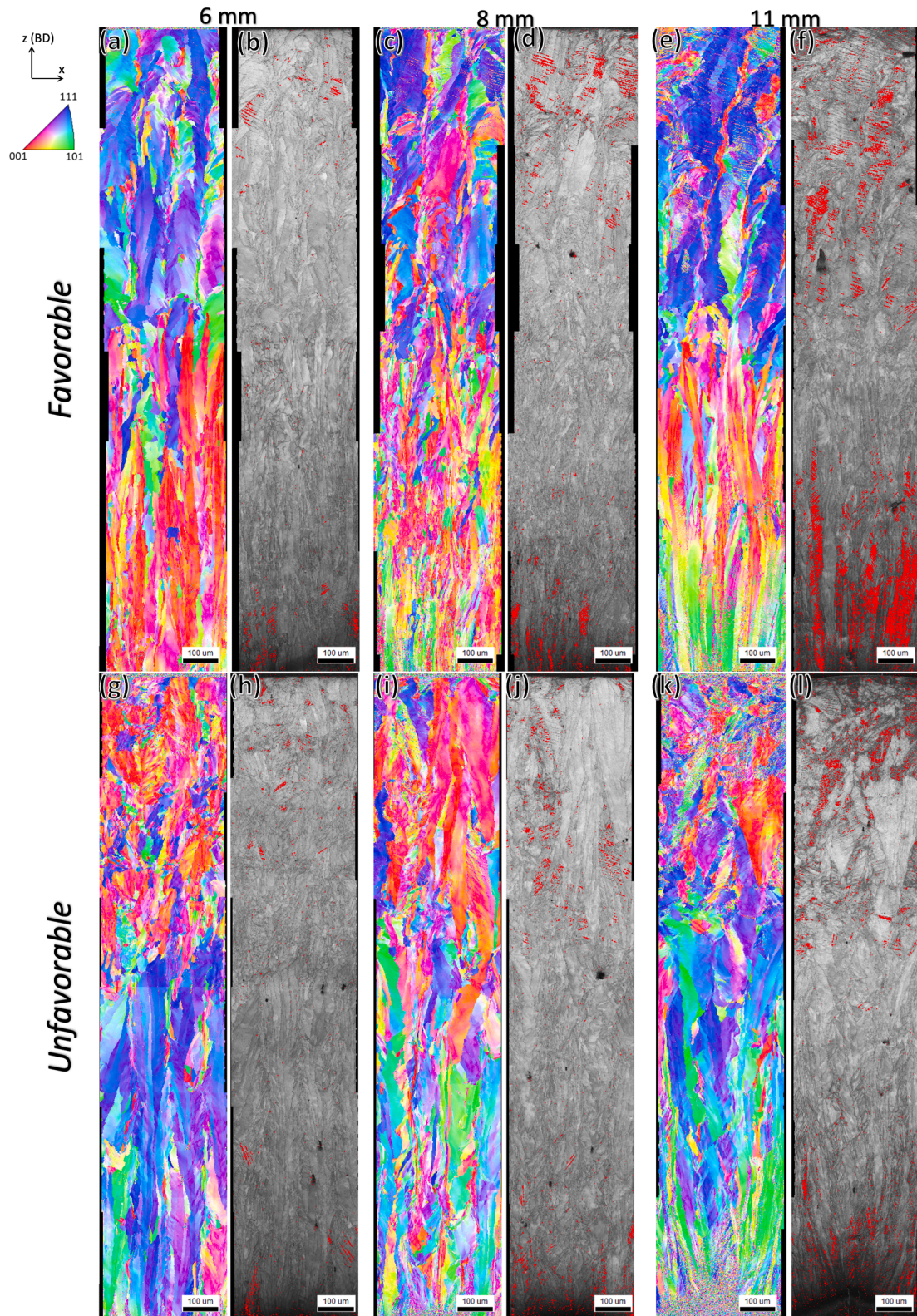


Fig. 6. EBSD orientation maps, along the x-direction, of the deformed microstructures of the favorable and unfavorable 316L L-PBF samples. (a,c,e) EBSD orientation maps with IPF coloring of the favorable sample after 6 mm, 8 mm and 11 mm of displacement. (g,i,k) EBSD orientation maps with IPF coloring for the unfavorable samples after 6 mm, 8 mm and 11 mm of displacement. (b,d,f) Image quality maps with the deformation twin boundaries highlighted red for the favorable sample after 6 mm, 8 mm and 11 mm displacement. (h,j,l) Image quality maps with the deformation twin boundaries highlighted red for the unfavorable sample after 6 mm, 8 mm and 11 mm displacement, respectively. The tensile side is on the top of the maps and the compressive side is at the bottom of the maps, for both samples.

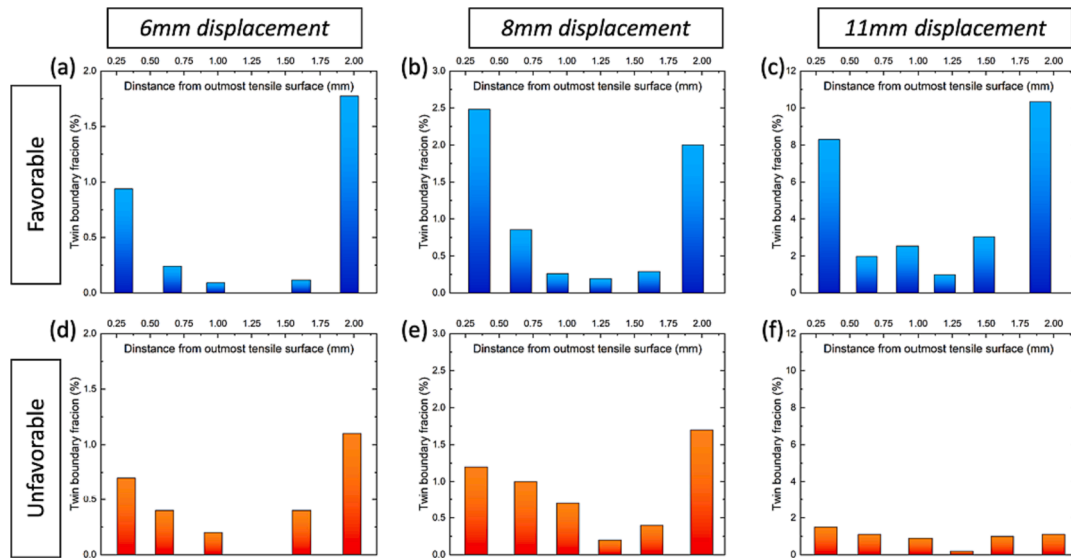


Fig. 7. Line fraction of deformation twins across the entire cross section of the samples, binned in sections of 0.25 mm thickness, for the favorable sample (a,b,c) and the unfavorable sample (d,e,f), after 6 mm, 8 mm and 11 mm displacement respectively.

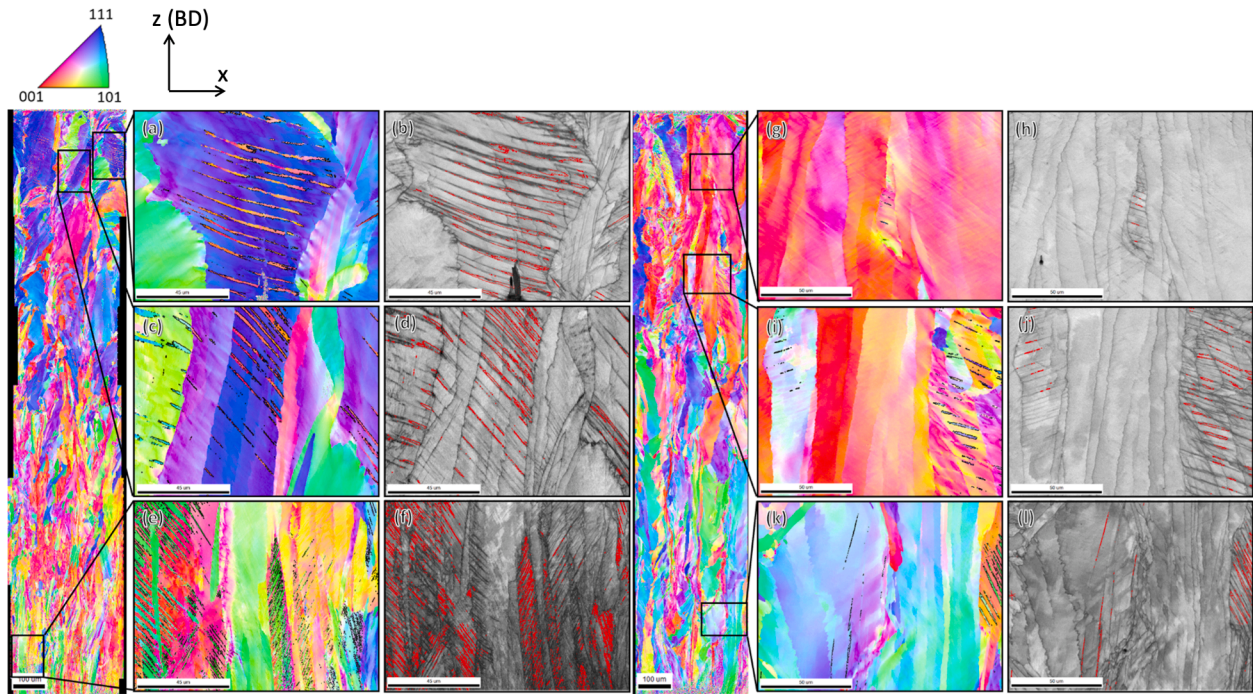


Fig. 8. High magnification EBSD orientation maps, with respect to the x-direction, with IPF coloring and grain boundary maps with the deformation twin boundaries highlighted red for the favorable (a–f) and unfavorable samples (g–l) at 8 mm displacement, on the tensile side (g–l). The tensile side is on the top of the maps and the compressive side is at the bottom of the maps, for both samples.

EBSD orientation maps, with IPF coloring along the x-direction, indicating local misorientation by dislocation-based plasticity. For instance, a detail of an unfavorable grain on the tensile side is shown in Fig. 9e, where the two slip systems with the highest Schmid factor for the given stress state are activated. Along the extensive dislocation slip in the unfavorable sample, limited twin activity can also be observed. In contrast to the favorable grains, the deformation twins in the unfavorable oriented ones are much thinner (Fig. 9d) and significantly suppressed (Fig. 8g–l).

4. Application to metastable austenitic steels

Besides the TWIP effect, the TRIP effect is also dependent on the crystallographic orientation, with respect to the loading direction. The mechanism of formation of strain-induced martensite in metastable austenitic steels is identical to the mechanism of twinning, where the dissociation of partial dislocations leads to the formation of ϵ -martensite, which is a precursor of α' -martensite. More details about the mechanisms of α' -martensite are provided in [33,42]. Therefore, on the tensile side, orientations close to the $\langle 111 \rangle$ axis favor the formation of martensite while orientations close to the $\langle 001 \rangle$ axis suppress the formation of martensite and vice-versa on the compressive side.

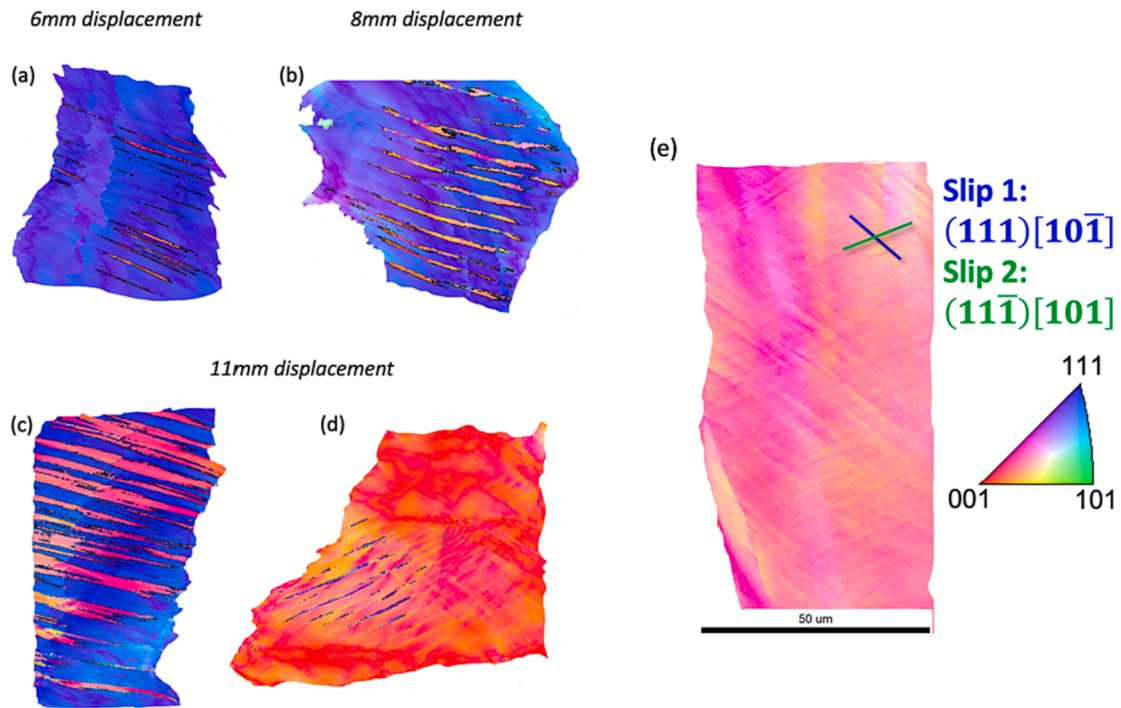


Fig. 9. (a)–(d) Evolution of the deformation twins, across the different amounts of displacement. At 6 mm and 8 mm the twins are enclosed within favorably oriented grains, while at 11 mm also unfavorably oriented grains exhibit twins. (e) Activated slip systems on an unfavorably oriented grain on the tension side of the specimen.

Moreover, it has been seen that minor changes in the crystallographic texture, inherited by the L-PBF process, can strongly impact the extend of the TWIP/TRIP effects in a medium stacking fault energy 304L material processed by L-PBF [33]. In the same context, two samples made of the same 304L powder as in the work by Sofras et al. [33], with favorable and unfavorable crystallographic textures, were V-bending tested and the results are shown in Fig. 10. It is observed again that the favorable sample exhibits higher energy dissipation capability compared to its unfavorable counterpart. The difference between the two samples, in terms of hardening and energy dissipation, is not as pronounced as in 316L though, due to the high nitrogen content that the 304L possess. As such, the TRIP effect is delayed [33], which has been observed under either uniaxial tension or compression. The application though to 304L showcases that besides TWIP effect, the TRIP effect can

also be tuned locally within single components and achieve improved mechanical behavior. Figs. S4 and S5 of the supplementary material show EBSD maps of the deformed 304L stainless steel sample where the co-existence of twins/ α' -martensite can be observed in the tensile side and ϵ -martensite/ α' -martensite in the compressive side which corroborates well with previous observation [33] under uniaxial tension and uniaxial compression.

5. Conclusions

Tailored bimodal parts of TWIP or TWIP/TRIP stainless steel were produced by laser powder bed fusion (L-PBF) and tested under V-bending. The study leverages on the site-specific microstructure manipulation that L-PBF enables and on the dependency of the

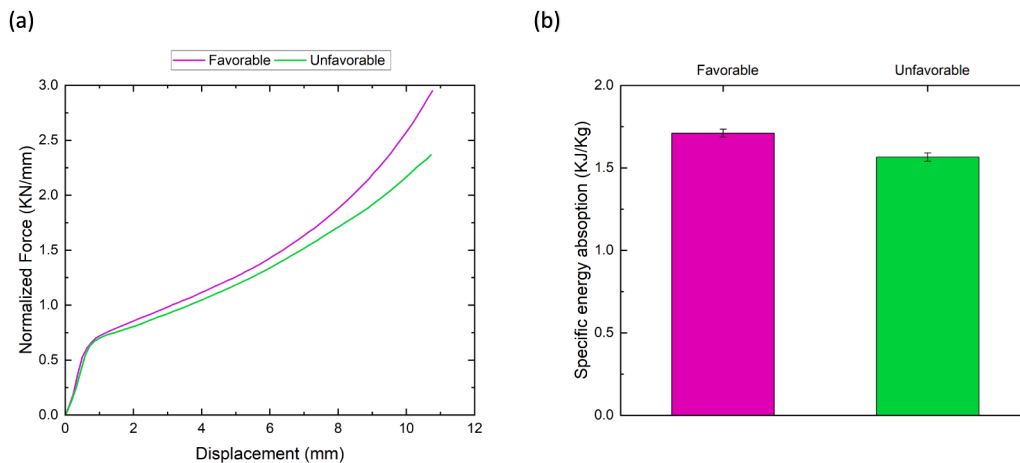


Fig. 10. Mechanical behavior of the L-PBF 304L stainless steel upon V-bending deformation. (a) Normalized force–displacement curves for the favorable and unfavorable samples. (b) Total dissipated energy shown as specific energy absorption at the end of deformation (until 11 mm displacement) for the favorable and unfavorable samples. The error bars represent the standard deviation among measurements for each sample.

deformation twinning and martensitic phase transformation on the crystallographic texture. The potentiality of L-PBF is demonstrated in a V-bending example, where plane strain tension and compression co-exist within a single part. The provided scripts allow for predicting the favorable and the unfavorable crystallographic textures along with the texture evolution for complex stress-states. The investigation highlights that with a synergy of simulations of the favorable orientations and the evolving crystallographic texture, one is able to tailor the crystallographic texture by appropriately choosing the L-PBF process parameters to match the stress state at hand. The tailored favorable microstructures exhibit up to 30 % more enhanced mechanical properties and energy absorption during V-bending, compared to other samples produced with the same process parameters (except for scanning direction). Massive twinning activity, leading to a superior mechanical response, is observed when a 316L sample is engineered with favorable microstructure for both tensile and compressive sides. In an identical sample, when the bending direction is flipped the work-hardening of the material is comparatively low, as the microstructure is unfavorable for extended twinning activity for both tensile and compressive sides. The study highlights the enormous potential of L-PBF as a tool for site-specific manipulation of the microstructure and realization of smart materials with enhanced mechanical properties and energy dissipation capabilities under complex stress states, using TWIP and/or TRIP austenitic stainless steels. This potentiality of L-PBF can be valuable in various applications, such as lattice and open cell structures, when one addresses the processing challenges of such intricate structures. However, it is demonstrated here that a priori knowledge via FEM can help identify local stress concentration and stress states within the components. As such, L-PBF can help locally enhance these areas in terms of mechanical properties and counteract local stress concentrations.

Author contributions

C.S. designed the experiments and performed the sample fabrication, FE modeling, EBSD characterization and wrote the paper. J.C. contributed to the sample preparation and EBSD investigation. X.L. contributed to the bending test and the analysis of the results. C.C.R. developed the bending setup, the FE model and helped with the FE modeling and the analysis of the results. C.L. provided the manufacturing means. R.L. and M.S. co-supervised the project. E.P. generated the idea, acquired the funding and supervised the project. All authors participated in the discussion and revision of the manuscript.

Declaration of competing interest

The authors declare that they have no known competing financial interests or personal relationships that could have appeared to influence the work reported in this paper.

Data availability

The raw data to reproduce the findings and the simulation scripts are available to download from: <https://doi.org/10.5281/zenodo.7553733>.

Acknowledgments

C.S. and E.P. acknowledge the financial support from the Swiss National Science Foundation (SNSF), Project number: 200021_188767. R. L. acknowledges the generous support of PX Group to the LMTM laboratory.

Appendix A. Supplementary data

Supplementary data to this article can be found online at <https://doi.org/10.1016/j.matdes.2023.112539>.

References

- [1] T. Zhang, Z. Huang, T. Yang, H. Kong, J. Luan, A. Wang, D. Wang, W. Kuo, Y. Wang, C.-T. Liu, In situ design of advanced titanium alloy with concentration modulations by additive manufacturing, *Science* (80-.). 374 (2021) 478–482. doi: 10.1126/science.abj3770.
- [2] C.J. Todaro, M.A. Easton, D. Qiu, D. Zhang, M.J. Birmingham, E.W. Lui, M. Brandt, D.H. StJohn, M. Qian, Grain structure control during metal 3D printing by high-intensity ultrasound, *Nat. Commun.* 11 (2020) 1–9, <https://doi.org/10.1038/s41467-019-13874-z>.
- [3] W. Xu, E.W. Lui, A. Pateras, M. Qian, M. Brandt, In situ tailoring microstructure in additively manufactured Ti-6Al-4V for superior mechanical performance, *Acta Mater.* 125 (2017) 390–400, <https://doi.org/10.1016/j.actamat.2016.12.027>.
- [4] P. Kürsteiner, M.B. Wilms, A. Weisheit, B. Gault, E.A. Jäggle, D. Raabe, High-strength Damascus steel by additive manufacturing, *Nature*. 582 (2020) 515–519, <https://doi.org/10.1038/s41586-020-2409-3>.
- [5] R. Cunningham, C. Zhao, N. Parab, C. Kantzos, J. Pauza, K. Fezzaa, T. Sun, A.D. Rollett, Keyhole threshold and morphology in laser melting revealed by ultrahigh-speed x-ray imaging, *Science* (80-.). 363 (2019) 849–852. doi: 10.1126/science.aav4687.
- [6] L. Liu, Q. Ding, Y. Zhong, J. Zou, J. Wu, Y.L. Chiu, J. Li, Z. Zhang, Q. Yu, Z. Shen, Dislocation network in additive manufactured steel breaks strength–ductility trade-off, *Mater. Today*. 21 (2018) 354–361, <https://doi.org/10.1016/j.mat.2017.11.004>.
- [7] J.H. Martin, B.D. Yahata, J.M. Hundley, J.A. Mayer, T.A. Schaedler, T.M. Pollock, 3D printing of high-strength aluminium alloys, *Nature*. 549 (2017) 365–369, <https://doi.org/10.1038/nature23894>.
- [8] Y.M. Wang, T. Voisin, J.T. McKeown, J. Ye, N.P. Calta, Z. Li, Z. Zeng, Y. Zhang, W. Chen, T.T. Roehling, R.T. Ott, M.K. Santala, P.J. Depond, M.J. Matthews, A. V. Hamza, T. Zhu, Additively manufactured hierarchical stainless steels with high strength and ductility, *Nat. Mater.* 17 (2018) 63–70, <https://doi.org/10.1038/NMAT5021>.
- [9] Y. Zhu, K. Zhang, Z. Meng, K. Zhang, P. Hodgson, N. Birbilis, M. Weyland, H. L. Fraser, S.C.V. Lim, H. Peng, R. Yang, H. Wang, A. Huang, Ultrastrong nanotwinned titanium alloys through additive manufacturing, *Nat. Mater.* 21 (2022) 1258–1262, <https://doi.org/10.1038/s41563-022-01359-2>.
- [10] Z. Li, Y. Cui, W. Yan, D. Zhang, Y. Fang, Y. Chen, Q. Yu, G. Wang, H. Ouyang, C. Fan, Q. Guo, D.B. Xiong, S. Jin, G. Sha, N. Ghoniem, Z. Zhang, Y.M. Wang, Enhanced strengthening and hardening via self-stabilized dislocation network in additively manufactured metals, *Mater. Today*. 50 (2021) 79–88, <https://doi.org/10.1016/j.mat.2021.06.002>.
- [11] S.H. Sun, T. Ishimoto, K. Hagihara, Y. Tsutsumi, T. Hanawa, T. Nakano, Excellent mechanical and corrosion properties of austenitic stainless steel with a unique crystallographic lamellar microstructure via selective laser melting, *Scr. Mater.* 159 (2019) 89–93, <https://doi.org/10.1016/j.scriptamat.2018.09.017>.
- [12] J. Zou, Y. Gaber, G. Voulazeris, S. Li, L. Vazquez, L.F. Liu, M.Y. Yao, Y.J. Wang, M. Holynski, K. Bongs, M.M. Attallah, Controlling the grain orientation during laser powder bed fusion to tailor the magnetic characteristics in a Ni-Fe based soft magnet, *Acta Mater.* 158 (2018) 230–238, <https://doi.org/10.1016/j.actamat.2018.07.064>.
- [13] R. Duan, S. Li, B. Cai, Z. Tao, W. Zhu, F. Ren, M.M. Attallah, In situ alloying based laser powder bed fusion processing of β Ti–Mo alloy to fabricate functionally graded composites, *Compos. Part B Eng.* 222 (2021), 109059, <https://doi.org/10.1016/j.compositesb.2021.109059>.
- [14] V.A. Popovich, E.V. Borisov, A.A. Popovich, V.S. Sufiarov, D.V. Masaylo, L. Alzina, Functionally graded Inconel 718 processed by additive manufacturing: Crystallographic texture, anisotropy of microstructure and mechanical properties, *Mater. Des.* 114 (2017) 441–449, <https://doi.org/10.1016/j.matdes.2016.10.075>.
- [15] S.G. Jeong, G.M. Karthik, E.S. Kim, A. Zargaran, S.Y. Ahn, M.J. Sagong, S.H. Kang, J.W. Cho, H.S. Kim, Architected heterogeneous alloys with selective laser melting, *Scr. Mater.* 208 (2022), 114332, <https://doi.org/10.1016/j.scriptamat.2021.114332>.
- [16] K.A. Sofinowski, S. Raman, X. Wang, B. Gaskey, M. Seita, Layer-wise engineering of grain orientation (LEGO) in laser powder bed fusion of stainless steel 316L, *Addit. Manuf.* 38 (2021), 101809, <https://doi.org/10.1016/j.addma.2020.101809>.
- [17] K. Sofinowski, M. Wittwer, M. Seita, Encoding data into metal alloys using laser powder bed fusion, *Addit. Manuf.* 52 (2022), 102683, <https://doi.org/10.1016/j.addma.2022.102683>.
- [18] J.J. Marattukalam, D. Karlsson, V. Pacheco, P. Beran, U. Wiklund, U. Jansson, B. Hjärvasson, M. Sahlberg, The effect of laser scanning strategies on texture, mechanical properties, and site-specific grain orientation in selective laser melted 316L SS, *Mater. Des.* 193 (2020), <https://doi.org/10.1016/j.matdes.2020.108852>.
- [19] M.P. Haines, M.S. Moyle, V.V. Rielli, V. Luzin, N. Haghdadi, S. Primig, Experimental and computational analysis of site-specific formation of phases in laser powder bed fusion 17–4 precipitate hardened stainless steel, *Addit. Manuf.* 73 (2023) 1–15, <https://doi.org/10.1016/j.addma.2023.103686>.
- [20] A. Arabi-Hashemi, X. Maeder, R. Figi, C. Schreiner, S. Griffiths, C. Leinenbach, 3D magnetic patterning in additive manufacturing via site-specific in-situ alloy modification, *Appl. Mater. Today*. 18 (2020), 100512, <https://doi.org/10.1016/j.apmt.2019.100512>.
- [21] I. Ferretto, A. Borzi, D. Kim, N.M.D. Ventura, E. Hosseini, W.J. Lee, C. Leinenbach, Control of microstructure and shape memory properties of a Fe–Mn–Si-based shape memory alloy during laser powder bed fusion, *Addit. Manuf. Lett.* 3 (2022), 100091, <https://doi.org/10.1016/j.addlet.2022.100091>.
- [22] W.A. Tiller, Preferred growth direction of metals, *Jom*. 9 (1957) 847–855, <https://doi.org/10.1007/bf03397928>.

- [23] M. Rappaz, Modelling of microstructure formation in solidification processes, *Int. Mater. Rev.* 34 (1989) 93–124, <https://doi.org/10.1179/imr.1989.34.1.93>.
- [24] M.S. Pham, B. Dovgvy, P.A. Hooper, C.M. Gourlay, A. Piglion, The role of side-branching in microstructure development in laser powder-bed fusion, *Nat. Commun.* 11 (2020) 1–12, <https://doi.org/10.1038/s41467-020-14453-3>.
- [25] O. Andreau, I. Koutiri, P. Peyre, J.D. Penot, N. Saintier, E. Pessard, T. De Terris, C. Dupuy, T. Baudin, Texture control of 316L parts by modulation of the melt pool morphology in selective laser melting, *J. Mater. Process. Technol.* 264 (2019) 21–31, <https://doi.org/10.1016/j.jmatprotec.2018.08.049>.
- [26] S.T. Methods, Standard Test Methods for Bend Testing of Material for Ductility 1, *Current.* 03 (1998) 1–7, <https://doi.org/10.1520/E0290-14>.
- [27] W. Chen, T. Voisin, Y. Zhang, J.B. Florien, C.M. Spadaccini, D.L. McDowell, T. Zhu, Y.M. Wang, Microscale residual stresses in additively manufactured stainless steel, *Nat. Commun.* 10 (2019) 1–12, <https://doi.org/10.1038/s41467-019-12265-8>.
- [28] Z. Sun, X. Tan, S.B. Tor, C.K. Chua, Simultaneously enhanced strength and ductility for 3D-printed stainless steel 316L by selective laser melting, *NPG Asia Mater.* 10 (2018) 127–136, <https://doi.org/10.1038/s41427-018-0018-5>.
- [29] X. Li, C.C. Roth, T. Tancogne-Dejean, D. Mohr, Rate- and temperature-dependent plasticity of additively manufactured stainless steel 316L: Characterization, modeling and application to crushing of shell-lattices, *Int. J. Impact Eng.* 145 (2020), 103671, <https://doi.org/10.1016/j.ijimpeng.2020.103671>.
- [30] L. Rémy, Interaction between slip and twinning systems and the influence of twinning on the mechanical behavior of fcc metals and alloys., *Metall. Trans. A, Phys. Metall. Mater. Sci.* 12 A (1981) 387–408. doi: 10.1007/bf02648536.
- [31] K. Lu, L. Lu, S. Suresh, Strengthening materials by engineering coherent internal boundaries at the nanoscale, *Science* (80-.). 324 (2009) 349–352. doi: 10.1126/science.1159610.
- [32] E. Polatidis, J. Čapek, A. Arabi-Hashemi, C. Leinenbach, M. Stroh, High ductility and transformation-induced-plasticity in metastable stainless steel processed by selective laser melting with low power, *Scr. Mater.* 176 (2020) 53–57, <https://doi.org/10.1016/j.scriptamat.2019.09.035>.
- [33] C. Sofras, J. Čapek, A. Arabi-Hashemi, C. Leinenbach, M. Frost, K. An, R.E. Logé, M. Stroh, E. Polatidis, Tailored deformation behavior of 304L stainless steel through control of the crystallographic texture with laser-powder bed fusion, *Mater. Des.* 219 (2022), <https://doi.org/10.1016/j.matdes.2022.110789>.
- [34] H.J. Kestenbach, The effect of applied stress on partial dislocation separation and dislocation substructure in austenitic stainless steel, *Philos. Mag.* 36 (1977) 1509–1515, <https://doi.org/10.1080/14786437708238531>.
- [35] T.S. Byun, On the stress dependence of partial dislocation separation and deformation microstructure in austenitic stainless steels, *Acta Mater.* 51 (2003) 3063–3071, [https://doi.org/10.1016/S1359-6454\(03\)00117-4](https://doi.org/10.1016/S1359-6454(03)00117-4).
- [36] H. Beladi, I.B. Timokhina, Y. Estrin, J. Kim, B.C. De Cooman, S.K. Kim, Orientation dependence of twinning and strain hardening behaviour of a high manganese twinning induced plasticity steel with polycrystalline structure, *Acta Mater.* 59 (2011) 7787–7799, <https://doi.org/10.1016/j.actamat.2011.08.031>.
- [37] I. Gutierrez-Urrutia, S. Zaefferer, D. Raabe, The effect of grain size and grain orientation on deformation twinning in a Fe-22wt.% Mn-0.6wt.% C TWIP steel, *Mater. Sci. Eng. A.* 527 (2010) 3552–3560, <https://doi.org/10.1016/j.msea.2010.02.041>.
- [38] I.V. Kireeva, Y.I. Chumlyakov, Z.V. Pobedennaya, I.V. Kuksgausen, I. Karaman, Orientation dependence of twinning in single crystalline CoCrFeMnNi high-entropy alloy, *Mater. Sci. Eng. A.* 705 (2017) 176–181, <https://doi.org/10.1016/j.msea.2017.08.065>.
- [39] I. Karaman, H. Sehitoglu, K. Gall, Y.I. Chumlyakov, H.J. Maier, Deformation of single crystal hadfield steel by twinning and slip, *Acta Mater.* 48 (2000) 1345–1359, [https://doi.org/10.1016/S1359-6454\(99\)00383-3](https://doi.org/10.1016/S1359-6454(99)00383-3).
- [40] J.K. Kim, M.H. Kwon, B.C. De Cooman, On the deformation twinning mechanisms in twinning-induced plasticity steel, *Acta Mater.* 141 (2017) 444–455, <https://doi.org/10.1016/j.actamat.2017.09.043>.
- [41] W.S. Choi, S. Sandlöbes, N.V. Malyar, C. Kirchlechner, S. Korte-Kerzel, G. Dehm, B. C. De Cooman, D. Raabe, Dislocation interaction and twinning-induced plasticity in face-centered cubic Fe-Mn-C micro-pillars, *Acta Mater.* 132 (2017) 162–173, <https://doi.org/10.1016/j.actamat.2017.04.043>.
- [42] E. Polatidis, W.-N.-N. Hsu, M. Šmíd, T. Panzner, S. Chakrabarty, P. Pant, H. Van Swygenhoven, Suppressed martensitic transformation under biaxial loading in low stacking fault energy metastable austenitic steels, *Scr. Mater.* 147 (2018) 27–32, <https://doi.org/10.1016/j.scriptamat.2017.12.026>.
- [43] C.C. Roth, D. Mohr, Ductile fracture experiments with locally proportional loading histories, *Int. J. Plast.* 79 (2016) 328–354, <https://doi.org/10.1016/j.jplas.2015.08.004>.
- [44] A.B. Kale, P. Alluri, A.K. Singh, S.H. Choi, The deformation and fracture behavior of 316L SS fabricated by SLM under mini V-bending test, *Int. J. Mech. Sci.* 196 (2021), 106292, <https://doi.org/10.1016/j.ijmecsci.2021.106292>.
- [45] F. Bachmann, R. Hielscher, H. Schaeben, Texture analysis with MTEX- Free and open source software toolbox, in: *Solid State Phenom.*, Trans Tech Publications Ltd, 2010: pp. 63–68. doi: 10.4028/www.scientific.net/SSP.160.63.
- [46] X. Wang, J.A. Muñoz-Lerma, M. Attarian Shandiz, O. Sanchez-Mata, M. Brochu, Crystallographic-orientation-dependent tensile behaviours of stainless steel 316L fabricated by laser powder bed fusion, *Mater. Sci. Eng. A.* 766 (2019), 138395, <https://doi.org/10.1016/J.MSEA.2019.138395>.
- [47] C. Bonatti, D. Mohr, Smooth-shell metamaterials of cubic symmetry: Anisotropic elasticity, yield strength and specific energy absorption, *Acta Mater.* 164 (2019) 301–321, <https://doi.org/10.1016/j.actamat.2018.10.034>.